Journal of Electroanalytical Chemistry 979 (2025) 118939

Contents lists available at ScienceDirect

Journal of Electroanalytical Chemistry

journal homepage: www.elsevier.com/locate/jelechem

Cabbage-like CoO/Ti_3C_2 with high cycling stability in lithium-ion storage

Dajun Wu [a,1,*], Xinyue Zhang [a,1], Xuan Wan [a], Heng Zhang [a], Zhicheng Wang [a], Shi Tao [a], Bin Qian [a], Shaohui Xu [b,*], Paul K. Chu [c]

[a] Jiangsu Laboratory of Advanced Functional Materials, School of Electronic and Information Engineering, Changshu Institute of Technology, Changshu 215500 China
[b] Key Laboratory of Polar Materials and Devices, Ministry of Education, and School of Physics and Electronic Science, East China Normal University, 500 Dongchuan Road, Minhang District, Shanghai 200241 China
[c] Department of Physics, Department of Materials Science and Engineering, and Department of Biomedical Engineering, City University of Hong Kong, Tat Chee Avenue, Kowloon, Hong Kong, China

ARTICLE INFO

Keywords:
Cobalt monoxide
Hydrothermal
Lithium ion battery
Ti_3C_2
Nanocomposites

ABSTRACT

Cobalt monoxide (CoO) has attracted much attention due to its high theoretical capacity and long cycling life in lithium-ion batteries (LIBs). However, the intrinsic CoO anode has poor conductivity and experiences large volume changes during cycling. The use of the proper carbide materials and morphological modification can overcome some of the barriers. In this work, few-layer Ti_3C_2 is used to fabricate the cabbage-like CoO/Ti_3C_2 composite by a one-step hydrothermal process, and the electrochemical properties of samples are evaluated systematically. The composite has a cabbage roll structure with a diameter of 2–7 μm assembled on folded nanosheets with a lateral dimension of 1–2 μm. The interlayer spacing is 0.1–0.5 μm and the Ti_3C_2 mass ratio is less than 9 %. The cabbage-like CoO/Ti_3C_2 electrode shows a high original specific capacity of 980.5 mAh g^{-1} at 0.5 C. After 1000 cycles, the reversible discharging capacity is still 598.1 mAh g^{-1} besides a good capacity retention ratio of 93.2 %. Compared with CoO and CoO/rGO, the cabbage-like CoO/Ti_3C_2 has a faster ion transport rate and robust skeleton, leading to excellent cycling stability. The simple fabrication strategy and materials with outstanding cycling stability have large potential in the development of next-generation LIBs.

1. Introduction

Transition metal oxides (TMOs) [1] such as MnO_2 [2], NiO [3], Fe_2O_3 [4], and CoO [5] have high theoretical specific capacities of 600–1200 mAh g^{-1} as anode materials in lithium-ion batteries (LIBs). In particular, CoO has garnered significant attention due to its high theoretical capacity, cost-effectiveness, and environmental friendliness [6–8]. However, the low conductivity and the structural instability of CoO cause serious capacity decay during cycling [9]. In this respect, nanoscale cobalt monoxide with the proper morphology and composition shows good results in energy storage and conversion applications. Although efforts have also been made to improve the properties by preventing aggregation of CoO-based materials, it is still challenging to further improve the energy density and produce CoO with a high capacity for anodes in LIBs. Techniques like nano-crystallization [10,11], doping [12 11,13], and compositing [14–16] are typically employed to enhance the specific capacity and cycling stability of CoO. For instance, Wan et al. [14] have fabricated layered mesoporous CoO/reduced graphene oxide (CoO/RGO), and the lithium-ion battery composed of CoO/RGO and an aqueous electrolyte shows a high discharge capacity of 2189.4 mAh g^{-1} at 100 mA g^{-1}. Yang et al. [5]. have prepared ZnO/CoO nanoclusters immobilized on *N*-doped 3D reduced graphene oxide by a solvothermal and freeze-drying method, and the capacity of $CoO_{1.2}$/$ZnO_{0.6}$-NrGO (6.78) is 600 mA h g^{-1} at 2.0 A g^{-1} after 1000 cycles. A bionic "flos albiziae" like CoO/SiO_2 heterostructure anode prepared on copper foam has a high reversible capacity of 1251 mAh g^{-1} after 250 cycles at 500 mA g^{-1} [17]. In order to improve the electrochemical properties, CoO-based composites comprising carbonaceous materials, metal oxide, carbide, and so on have been proposed for anodes in LIBs.

Two-dimensional (2D) titanium carbide such as Ti_3C_2, a type of MXene transition metal carbide, has been explored as an anode in LIBs due to its unique layered structure, excellent hydrophilicity, good conductivity, and favorable Li^+ intercalation [18]. However, there are four major limitations of 2D MXene electrodes, including self-stacking, low

* Corresponding authors.
E-mail addresses: 201700028@cslg.edu.cn (D. Wu), 050522137@cslg.edu.cn (X. Zhang), 050523142@cslg.edu.cn (X. Wan), wangzc@cslg.edu.cn (Z. Wang), taoshi@cslg.edu.cn (S. Tao), njqb@cslg.edu.cn (B. Qian), shxu@ee.ecnu.edu.cn (S. Xu), paul.chu@cityu.edu.hk (P.K. Chu).
[1] The two co-first authors contributed equally to the work.

https://doi.org/10.1016/j.jelechem.2025.118939
Received 31 October 2024; Received in revised form 8 December 2024; Accepted 10 January 2025
Available online 11 January 2025

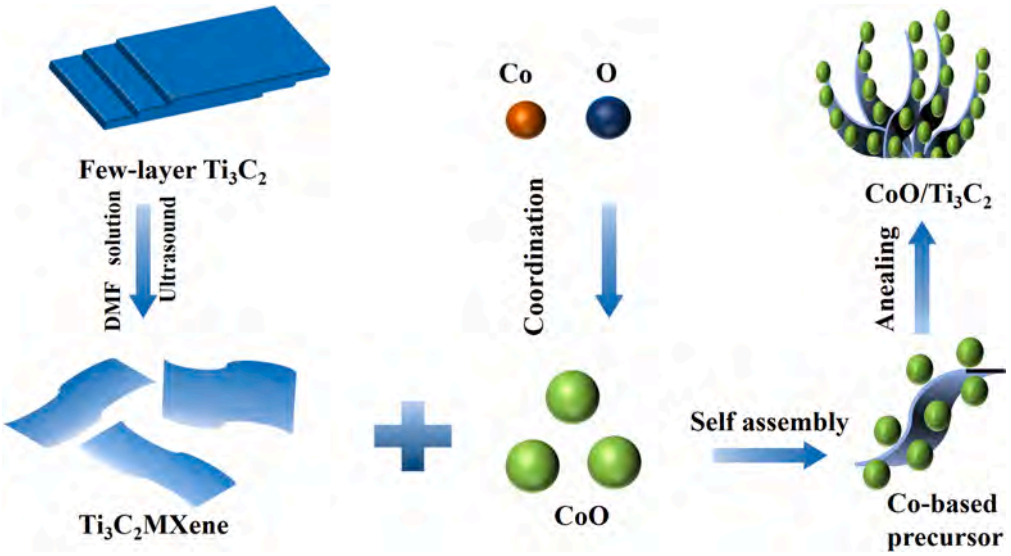

Fig. 1. Schematic illustration of the synthesis of cabbage-like CoO/Ti_3C_2.

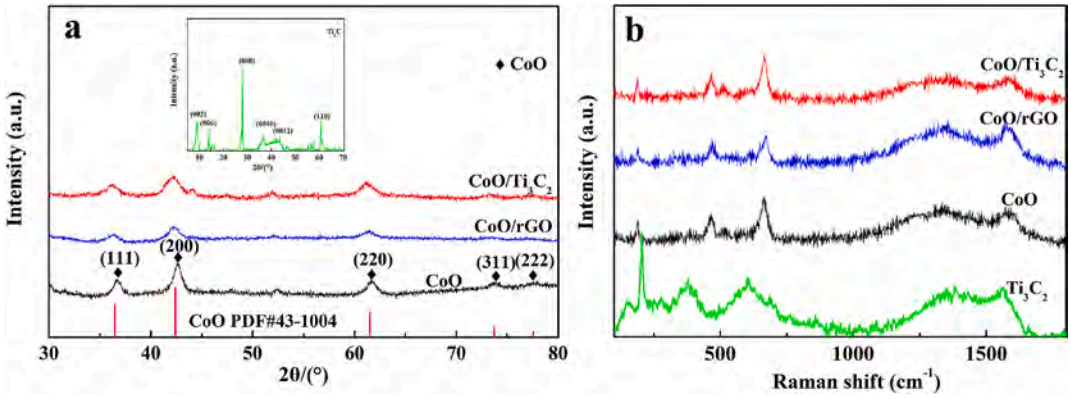

Fig. 2. (a) XRD patterns and (b) Raman scattering spectra of Ti_3C_2, CoO, CoO/rGO, and CoO/Ti_3C_2.

specific surface area, and disturbance of Li^+ diffusion by surface terminations [19]. To overcome these hurdles plaguing hierarchical Ti_3C_2-based composites, heteroatom doping and coatings (sulfide, hydroxide, carbon, etc.) have been proposed, for example, Ti_3C_2/@Si@N [20], $SnO_2/Ti_3C_2T_x$ [21], TiO_2/Ti_3C_2 [22], Ti_3C_2/VN@C [23], Ti_3C_2/NiFe-LDH [24], SiO_2/Ti_3C_2 [25], SnS/Ti_3C_2 [26], and Ni-MOF/Ti_3C_2 [27]. Furthermore, Ti_3C_2 and cobalt oxide nanostructures had been researched, such as CoO/Ti_3C_2 [28], Ti_3C_2@CoO/ZnO [29], Co-MOF/$Ti_3C_2T_x$ [30], $Co_3O_4/Ti_3C_2T_x$ [31], and $Ti_3C_2T_x$/CoNi-MOF [32]. For instance, Zhu et al. [28] have used a hydrothermal technique to introduce CoO nanoparticles to increase the surface areas of Ti_3C_2 and prevent the aggregation of Ti_3C_2. Compared to CoO or Ti_3C_2 alone, CoO/Ti_3C_2 has a larger initial discharge capacity of 1389 mAh g^{-1} with a Coulombic efficiency of 61 % at 100 mA g^{-1}. After 100 cycles, the reversible capacity remains at 313 mAh g^{-1}. Tang et al. [29] have anchored CoO/ZnO nanodots onto Ti_3C_2 to address self-stacking and increase the surface area, resulting in a specific capacity of 627 mAh g^{-1} at a high current density of 1 A g^{-1} for 300 cycles.

Most of these studies have primarily focused on enhancing the electrochemical properties by depositing CoO coatings on Ti_3C_2. Virtually, precise control of the morphology of CoO/Ti_3C_2 is crucial to the surface area and cycling characteristics [33]. To the best of our knowledge, the use of few-layer Ti_3C_2 as a conductive agent to control morphology of CoO-based composites are still scarcely reported. Herein, the cabbage-like CoO/Ti_3C_2 composite is prepared by a hydrothermal process and annealing. The cabbage (2–5 μm) structure consists of few-layer Ti_3C_2 nanosheets and CoO nanoparticles (20–30 nm) with an interlayer spacing of 0.5–1 μm. The few-layer Ti_3C_2 nanosheets envelop the CoO nanoparticles to reduce direct contact with the electrolyte and improve the Coulombic efficiency and cycling stability. Compared to CoO and CoO/rGO, CoO/Ti_3C_2 has better Li-ion storage properties and stability as anodes in LIBs. This simple and scalable technique has large potential in the development of advanced CoO-based anodes in LIBs.

2. Experimental details

2.1. Chemicals and materials

All the chemical reagents were analytical grade and used without purification. Cobalt nitrate ($Co(NO)_3{\cdot}6H_2O$), ammonium fluoride (NH_4F), urea ($CO(NH_2)_2$), and sodium dodecyl benzene sulfonate (SDBS) powder were purchased from Aladdin Reagents and few-layer Ti_3C_2 MXene, reduced graphene oxide (rGO) and the other reagents were obtained from Sinopharm Chemical Reagents Co. Ltd. Deionized water (18 MΩ) was used in the experiments.

2.2. Synthesis of CoO/Ti_3C_2

The cabbage-like CoO/Ti_3C_2 composite was prepared hydrothermally. In brief, 0.58 g of $Co(NO_3)_2{\cdot}6H_2O$, 0.07 g of NH_4F, 0.24 g of CO

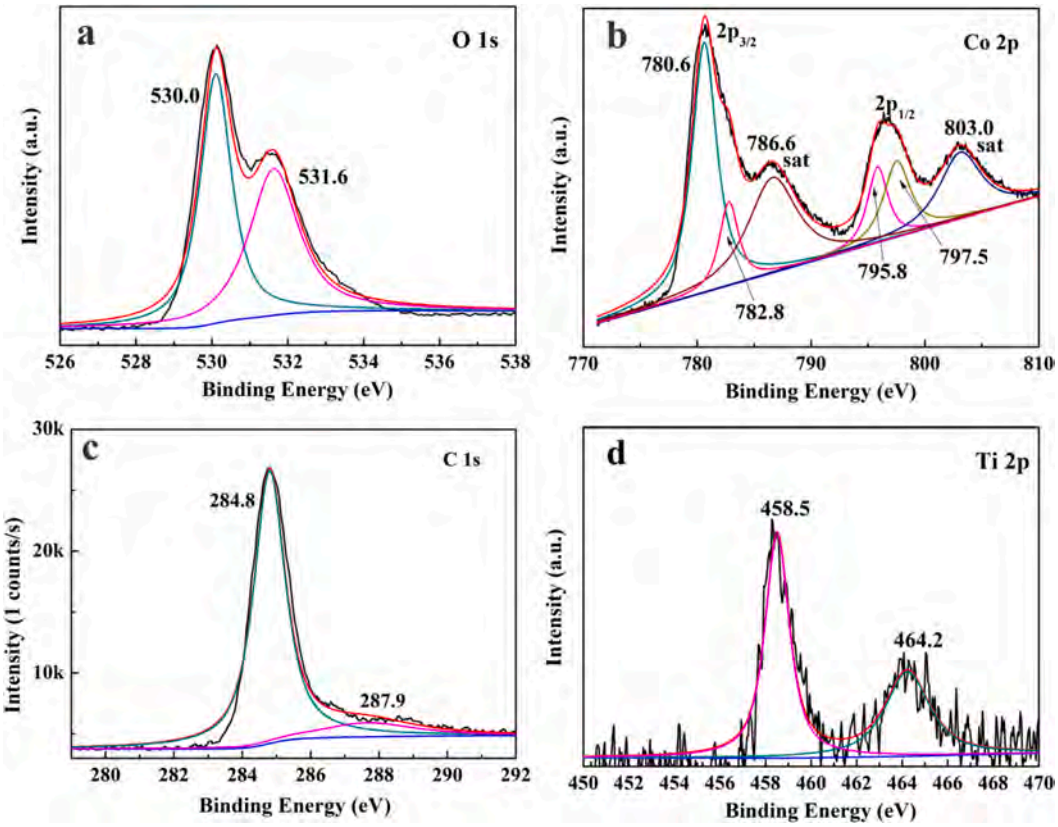

Fig. 3. XPS spectra of CoO/Ti_3C_2: (a) O 1*s*, (b) Co 2*p*, (c) C 1*s*, and (d) Ti 2*p*.

$(NH_2)_2$, and 0.20 g of SDBS powder were added to 35 ml of deionized water and stirred for half an hour until the solution turned pink. The solution was transferred to a 50 ml Teflon-lined stainless-steel autoclave containing 2.8 ml of the few-layer Ti_3C_2 dispersion (5 mg/ml). The sealed autoclave was heated to 120 °C for 8 h and after cooling to room temperature, the product was centrifuged with deionized water and ethanol until the pH was 7, followed by vacuum-drying for 10 h at 80℃ to produce the precursor. The precursor was then calcined at 500 °C for 2 h under argon to produce CoO with the layered structure. For comparison, the same procedure was adopted for the synthesis of CoO in the absence of Ti_3C_2 and CoO/rGO with 5 drops of the GO dispersion (5 mg/ml).

2.3. Assembly of LIBs and electrochemical assessment

The lithium-ion battery was assembled in a 2032-type button cell in an argon-filled glove box. A mixture of CoO/Ti_3C_2 (or CoO, CoO/rGO) powder, acetylene black, and polyvinylidene difluoride (PVDF) in *N*-methyl pyrrolidone (NMP) was mixed with a weight ratio of 8:1:1. After stirring for 4 h, the slurry was placed on a Cu foil and dried overnight at 60 °C in a vacuum oven. The counter electrode was a bare Li-metal foil. The electrolyte was 1 M $LiPF_6$ in diethyl carbonate (DEC)/ethylene carbonate (EC) (volume ratio 1:1), and a Celgard 2300 membrane was the separator. The LAND CT2001A system was used to conduct galvanostatic charging-discharging (GCD). The CHI760E (Chenhua, Shanghai) electrochemical workstation was employed for cyclic voltammetry (CV) and electrochemical impedance spectroscopy (EIS). To enhance the wettability of the cell components and achieve a stable potential, the cells were aged for 12 h before the charging-discharging measurement. CV and GCD were carried out in the potential window between 0.01 and 3.00 V (vs. Li/Li^+) at room temperature. EIS was conducted at the open circuit potential (OCP) with an amplitude of 5 mV in the frequency range between 10^5 and 10^{-2} Hz.

3. Results and discussion

The cabbage-like CoO/Ti_3C_2 is prepared by a hydrothermal process and annealing as illustrated in Fig. 1. Cobalt nitrate, ammonium fluoride, urea, and SDBS are added to deionized water during synthesis, and the SDBS template controls the product morphology and crystal formation [40]. As shown by our previous experiments, few-lay Ti_3C_2 nanosheets have many oxygen-containing surface groups thus producing superior dispersive properties and adsorption in the aqueous solution. The few-layer Ti_3C_2 nanosheets effectively absorb Co ions during crystal nucleation and growth of the CoO precursor. Afterward, the precursor is calcined under argon atmosphere, carbonized, and crystallized to produce the final product of cabbage-like CoO/Ti_3C_2.

The structure and phase of CoO, CoO/rGO, and CoO/Ti_3C_2 are characterized by X-ray diffraction (XRD). As shown in Fig. 2a, the peaks at 36.6°, 42.5°, 61.5°, 73.7°, and 77.6° correspond to the (1 1 1), (2 0 0), (2 2 0), (3 1 1), and (2 2 2) planes of CoO (JCPDS 431004) [17]. But the concentration of rGO, Ti_3C_2 is less than 5 %, so it cannot be detected by XRD. The Ti_3C_2 sample exhibits typical diffraction peaks with the (0 0 2) plane, which are the same as the reported works [22].

Raman scattering is performed to analyze the structure of CoO, CoO/rGO, and CoO/Ti_3C_2. As shown in Fig. 2b, the peaks at 192 cm^{-1} and 600 cm^{-1} correspond to the F_{2g} vibrational mode of CoO, while those at 440 cm^{-1} and 680 cm^{-1} are the F_g and A_{1g} modes of CoO, respectively [14]. Four peaks are observed below 1000 cm^{-1} from CoO/Ti_3C_2 and CoO/rGO [28] showing the CoO phase. The two broad peaks between 1200 and 1800 cm^{-1} are the D- and G-peaks of graphitic carbon. Compared with the pure CoO and CoO/rGO, the intensities of the D-peak at 1300 cm^{-1} and G-peak at 1570 cm^{-1} of CoO/Ti_3C_2 increase because of the insertion of CoO between the layers of Ti_3C_2 and more exposed C on the surface, which are consistent with the XRD results. These surface defect sites provide more active sites for electron storage.

Fig. 3 shows that CoO/Ti_3C_2 contains O, Co, C, and Ti consistent with

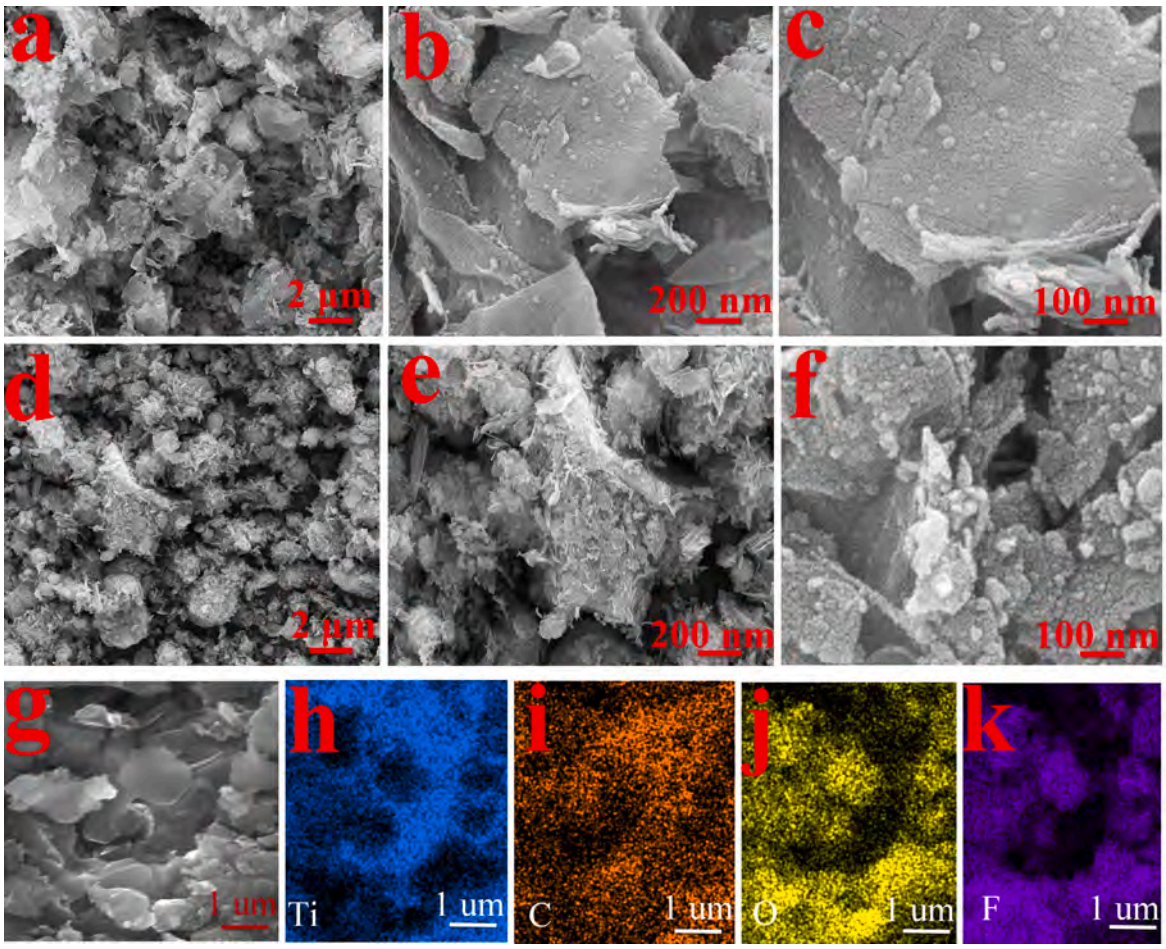

Fig. 4. SEM images of (a–c) CoO and (d–f) CoO/rGO; (g–k) SEM image and elemental maps of Ti_3C_2.

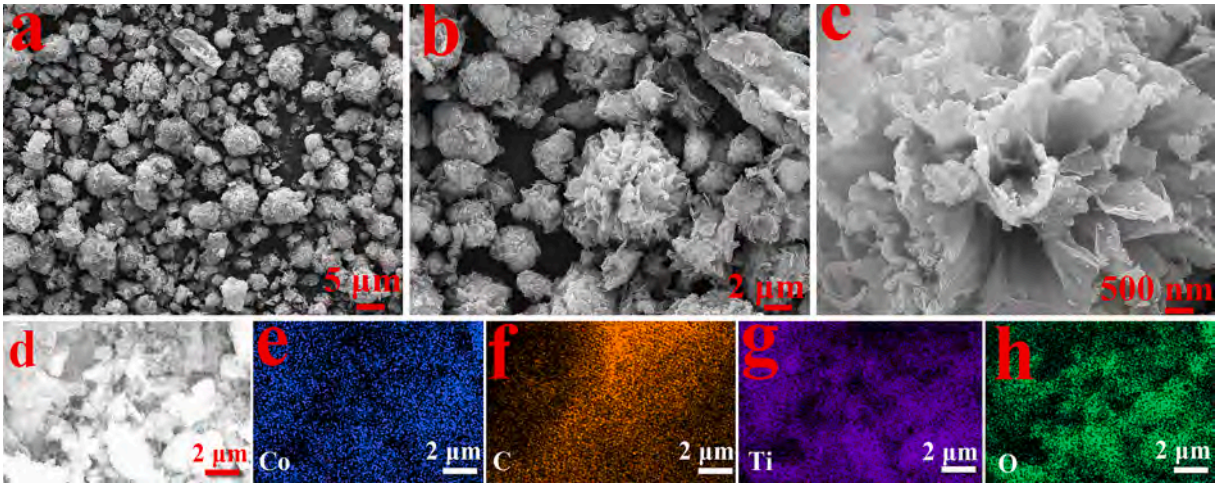

Fig. 5. SEM images of (a–c) CoO/Ti_3C_2 and (d–h) SEM image elemental maps of CoO/Ti_3C_2.

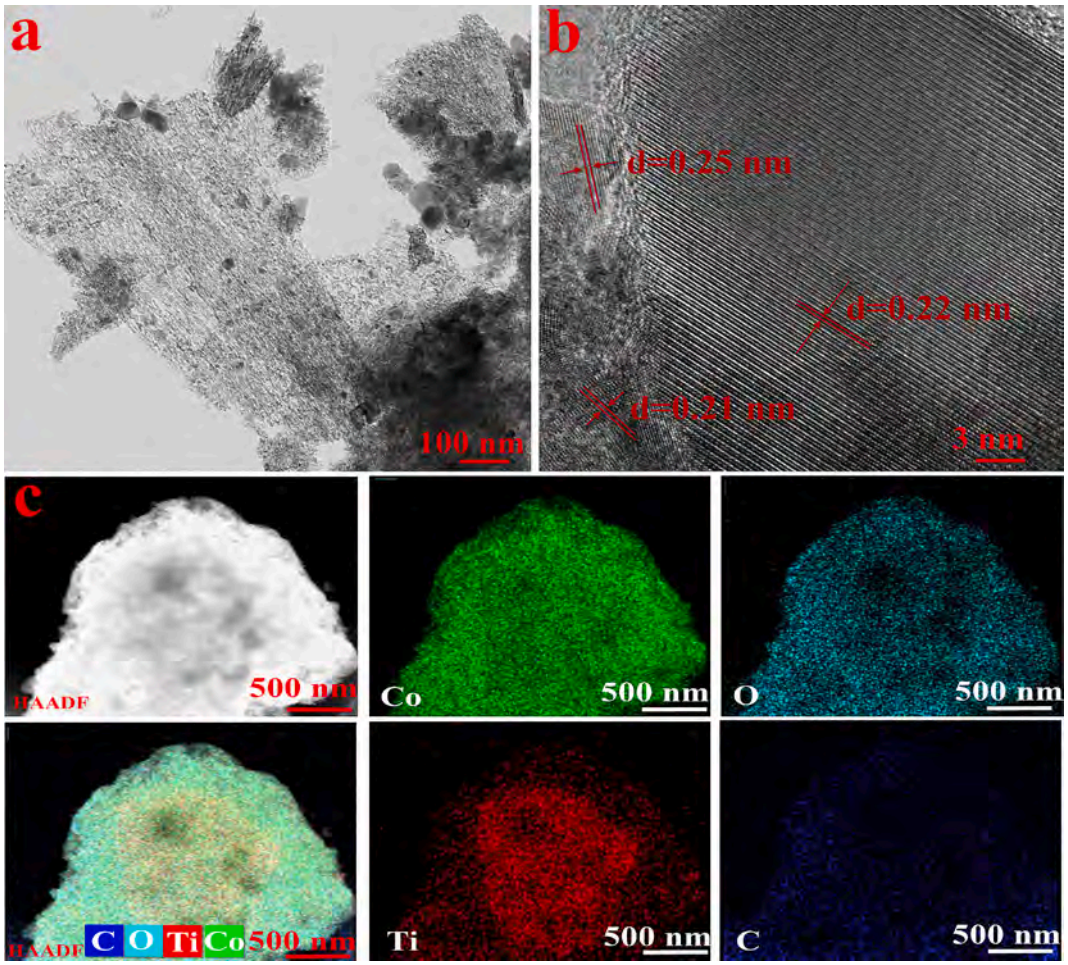

Fig. 6. (a–b) TEM and HR-TEM images of CoO/Ti_3C_2; (c) HAADF image of CoO/Ti_3C_2 and EDS elemental maps of Co, O, Ti, C.

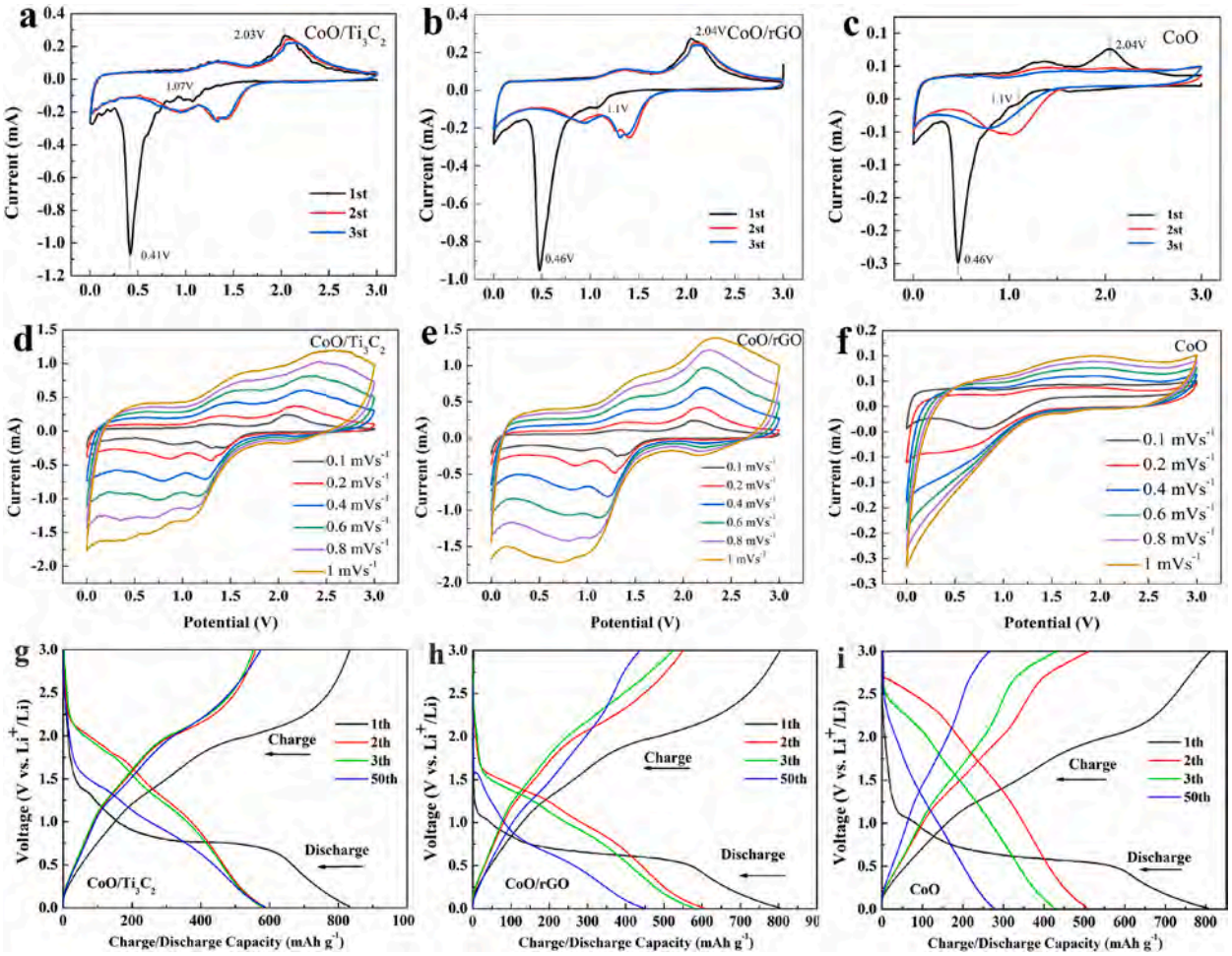

Fig. 7. 1st, 2nd, and 3rd cycles CV curves of (a) CoO/Ti_3C_2, (b) CoO/rGO, and (c) CoO at a scanning rate of 0.1 mVs^{-1}; CV curves of (d) CoO/Ti_3C_2, (e) CoO/rGO, and (f) CoO at scanning rates of 0.1, 0.2, 0.4, 0.8 and 1 mV s^{-1}; Charging and discharging curves of the first 3rd and 50th cycles of (g) CoO/Ti_3C_2, (h) CoO/rGO and (i) CoO.

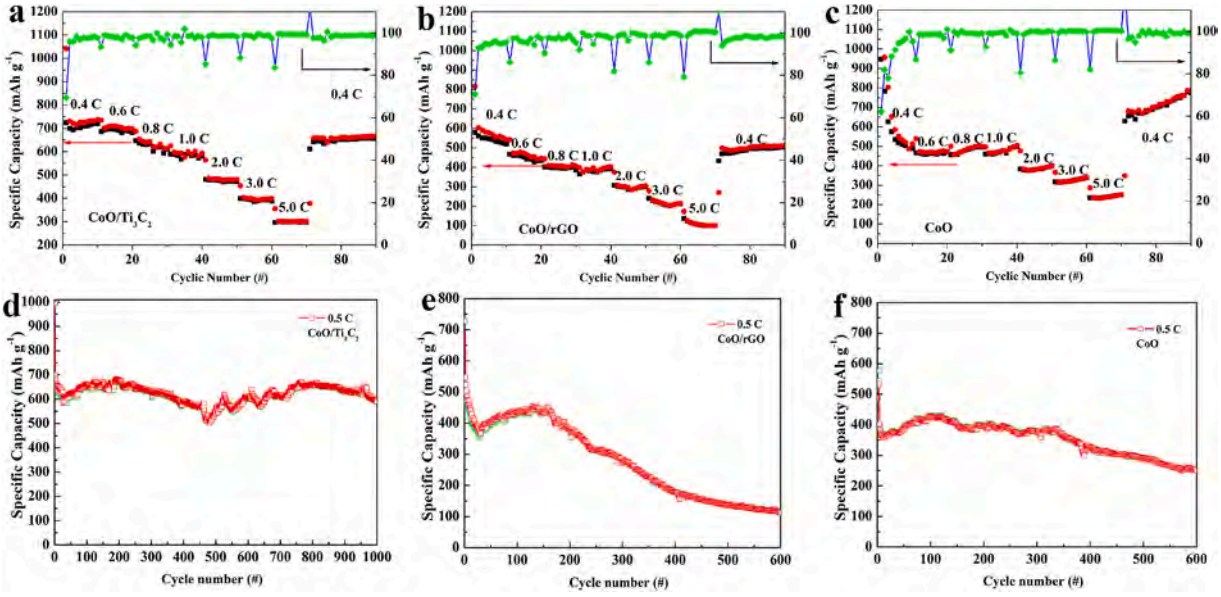

Fig. 8. Rate curves of (a) CoO/Ti_3C_2, (b) CoO/rGO, and (c) CoO; Cycling curves of (a) CoO/Ti_3C_2, (b) CoO/rGO, and (c) CoO.

Table 1
Comparison of the specific capacities of Co-based electrodes.

Materials	Specific capacity	Current Densities	After cycles	Retention ratios	References
CoO@CC	145 $mAhg^{-1}$	0.1 A g^{-1}	500	86.4 %	[11]
CoO@PAN	72.8 $mAhg^{-1}$	10 C	1000	96.1 %	[15]
CoO/SnO_2	1251 $mAhg^{-1}$	0.5 A g^{-1}	250	120 %	[17]
CoO/Ti_3C_2	324 $mAhg^{-1}$	0.1 A g^{-1}	100	99 %	[28]
CoO/rGO	1167 $mAhg^{-1}$	5 A g^{-1}	40	76 %	[14]
Co@MXene/CNF	422.8 $mAhg^{-1}$	1 A g^{-1}	500	99 %	[39]
Ti_3C_2@CoO/ZnO	327 $mAhg^{-1}$	1 A g^{-1}	300	120 %	[29]
CoO @TiO_2/C	1136 $mAhg^{-1}$	0.5 A g^{-1}	200	110 %	[16]
Cabbage-like CoO/Ti_3C_2	**598.1 $mAhg^{-1}$**	**0.5 C**	**1000**	**93.2 %**	**This work**

XRD and Raman scattering. The O 1*s* peaks of CoO/Ti_3C_2 at 531.6 and 530.0 eV stem from Co-O in CoO. For the quantitative calculation of the mass ratio of Ti to Co element in CoO/Ti_3C_2, we integrated the XPS pattern area for each element, showing the mass ratio of Ti to Co element is 1:8. Fig. 3b shows that the Co 2*p* spectrum of CoO/Ti_3C_2 has two main peaks at 780.6 and 797.5 eV with a spin orbital splitting energy of 16.9 eV [8,12]. Likewise, the Co $2p_{3/2}$ peaks at 780.6 eV are characteristic of Co^{3+}, while the two shake-up satellite peaks at 786.6 and 803.0 eV indicate spinel cobaltite. Generally, the satellite peak at 786.6 eV is ascribled to Co^{2+} and that at 803.0 eV shows Co^{3+}. Hence, CoO/Ti_3C_2 is composed of $Co^{2+/3+}$ on the surface. The C 1*s* spectrum can be deconvoluted into three peaks at 287.9 and 284.8 eV associated with C–OO and C sp^2 (Fig. 3c), respectively. Deconvolution of Ti $2p^{1/2}$ and Ti $2p^{3/2}$ shows two peaks corresponding to Ti–C at (464.2 eV) and Ti–O (at 458.5 eV) (Fig. 3d) [25]. These results reveal more surface defects, which are expected to improve the surface area and electrochemical properties. As we know that ICP-OES is a simple and rapid method in element analysis. The ICP-OES result (Ti of 24.5 mg/L and Co of 196 mg/L) suggests that the Ti to Co element mass ratio of CoO/Ti_3C_2 is also about 1:8, and then mole ratio of Ti to Co is about 3:20, indicating the Ti_3C_2 percentage of the total is ~ 9 %, which are consist with the results of XPS.

As shown in Figs. 4–5, the SEM images reveal that the flake-shape CoO is composed of nanoparticles with a length of 0.5 ~ 1 μm (Fig. 4a–c). In CoO/rGO, the CoO nanoparticles are uniformly coated on the surface of rGO (Fig. 4d–f) to improve the surface area and conductivity. Fig. 4g–k disclose the few-layer structure of Ti3C2 MXene with a length of 1 ~ 2 μm. Energy-dispersive X-ray spectroscopy (EDS) mapping shows uniform elemental distributions of Ti/C/O/F on Ti_3C_2. The oxygen-containing surface groups of Ti_3C_2 MXene produce superior dispersive properties and adsorption in the aqueous solution. Compared to CoO and CoO/rGO, CoO/Ti_3C_2 has a cabbage-like structure (Fig. 5a–c). The cabbage structure (2–5 μm) consists of few-layer Ti_3C_2 nanosheets and CoO nanoparticles (20–30 nm) with an interlayer spacing of 0.5–1 μm. EDS mapping provides evidence that Co, C, Ti, and O are well dispersed on CoO/Ti_3C_2 (Fig. 5d–h).

The TEM and HR-TEM images of CoO/Ti_3C_2 are depicted in Fig. 6a–b. The CoO/Ti_3C_2 nanobelts are composed of numerous nanoflakes with a length of ~1 μm and a width of 200 nm. The cabbage-like structure contains nanobelts with a micro-wrinkle structure for efficient support and more active surface sites. The CoO nanoparticles are incorporated uniformly into the few-layer Ti_3C_2 nanoflakes. As shown by the HR-TEM image of CoO/Ti_3C_2 (Fig. 6b), the inter-planar distances, d, are 0.24 nm and 0.21 nm, corresponding to the (2 2 0) and (2 0 0) planes of CoO [34]. The lattice stripe spacing of 0.22 nm aligns precisely with the (1 0 4) crystal plane of Ti_3C_2 [35], thus affirming the successful synthesis of CoO/Ti_3C_2.

To determine the electrochemical properties, CV is conducted between 0.01 and 3.00 V at a scanning rate of 0.1 mV/s (in Fig. 7a–c). In the first cycle, two cathodic peaks are observed, a sharp one at 0.41 ~ 0.46 V and a small one at 1.07 ~ 1.01 V, which are related to Co^{2+} to Co, formation of SEI (solid electrolyte interphase), and irreversible electrolyte decomposition. The two broad peaks at 1.25 V and 2.04 V arise from metallic Co to Co^{2+} as well as Co^{2+} to Co^{3+} during anodic oxidation, respectively. The other cycles almost overlap. The cathodic peak, which moves to 1.0 V, is associated with the formation of the Li_xCoO phase, demonstrating the good reversible capability and high stability of CoO/Ti_3C_2. In the subsequent cycles, compared with other electrodes, the CV curves of CoO/Ti_3C_2 are more stable, indicating that the redox reactions taking place on the anode are reversible. CoO/Ti_3C_2 has smaller and different redox values of 0.38 and 0.63 V, indicating that CoO/Ti_3C_2 has high reversible capacity and good stability. Fig. 7d–f show the CV curves of CoO/Ti_3C_2, CoO/rGO, and CoO anodes at different scanning rates from 0.1 to 1 mV/s. Compared with other electrodes, the CV curves of CoO/Ti_3C_2 do not change significantly as the scanning rates increase [36] consequently demonstrating good reversibility.

The 3rd and 5th CV cycles of CoO/Ti_3C_2, CoO/rGO, and CoO are shown in Fig. 7g–i. The first GCD curve exhibits a noticeable plateau at 0.8 V (CoO/Ti_3C_2), 0.7 V (CoO/rGO), and 1.25 V (CoO), respectively, due to the solid electrolyte interphase (SEI) layer and interactions of CoO and Li^+ [37,38]. The initial discharging capacities of CoO/Ti_3C_2, CoO/rGO, and CoO are 840.1 mAh g^{-1}, 798.3 mAh g^{-1}, and 802.4 mAh g^{-1}, respectively. After 50 cycles, the reversible capacities of CoO/Ti_3C_2, CoO/rGO, and CoO are 590.8 mAh g^{-1}, 447.6 mAh g^{-1} and 270.4 mAh g^{-1}, respectively. The results confirm that the synergistic effects of CoO nanoparticles and few-layer Ti_3C_2 MXene improve the specific capacity and rates.

Fig. 8a–c show the rates of CoO/Ti_3C_2, CoO/rGO and CoO. The cabbage-like CoO/Ti_3C_2 achieves a substantial capacity of 724.5 mAh g^{-1} at 0.4 C. When the rate of discharge changes from 0.4 to 5.0 C, the rechargeable capacities of the cabbage-like CoO/Ti_3C_2 nanocomposite are 724.5, 705.4, 651.2, 603.3, 481.9, 400.7, and 300.6 mAh g^{-1}. Hence, CoO/Ti_3C_2 shows enhanced Li-ion diffusion and electron transfer, leading to rate capabilities and reaction kinetics.

The enhanced Li^+ storage capacity can be attributed to the synergetic effects between CoO and few-layer Ti_3C_2. Fig. 8d–f show the cycling results at 0.5 C. After 1,000 cycles, the discharging capacity of the cabbage-like CoO/Ti_3C_2 electrode is still 598.1 $mAhg^{-1}$ in addition to good capacity retention ratios of 93.2 % at 0.5 C, which are better than those of CoO/rGO (140.1 $mAhg^{-1}$, 28.2 %) and CoO (260.2 $mAhg^{-1}$, 68.4 %) after 600 cycles. The cycling properties of CoO/Ti_3C_2 are better than those of other CoO-based materials reported in the literature, including CoO/Ti_3C_2 [28], CoO/rGO [14], and Co@MXene/CNF [39], as shown in Table 1. The inverse cycle curves of CoO/Ti_3C_2 indicate faster ion transfer and the conductive network enhances the cycling stability of Co-based materials.

To check the morphology of the active materials after the cycling test, we disassemble the electrode of CoO/Ti_3C_2 after 1000 cyles in Fig. 9a–b. The structure of the CoO/Ti_3C_2 are robust enough to retain the structural integrity and order, and the CoO/Ti_3C_2 composites are intact, keeping the original morphology and construct. Fig. 9c–d shows the Nyquist plots of the cabbage-like CoO/Ti_3C_2, CoO/rGO, and CoO electrodes revealing a semicircle in the mid-to-high frequency region representing the charge transfer resistance and a sloping line in the low-frequency region [41–43]. The R_{ct} values of CoO/Ti_3C_2, CoO/rGO, and CoO are 85.3 Ω, 155.2 Ω, and 1.0 k Ω, respectively, indicating that Ti_3C_2 reduces the charge transfer impedance of CoO. The XRD of CoO/Ti_3C_2 electrode after 1000 cycles in Fig. 9e, revealing the structure of the CoO/Ti_3C_2 retain the original structure supporting the well stability cycles. All in all, the excellent electrochemical properties of CoO/Ti_3C_2

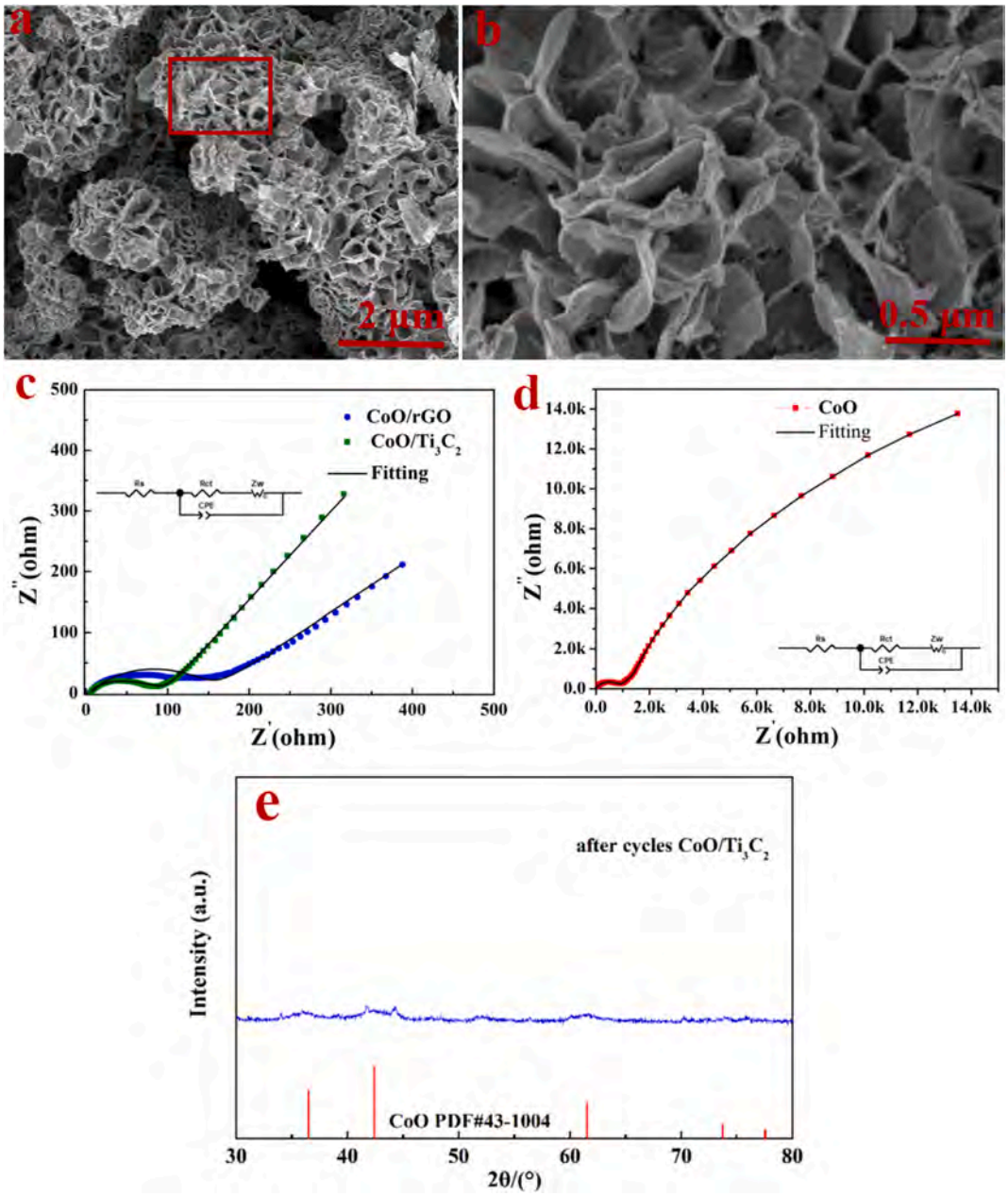

Fig. 9. (a–b)The morphology of the CoO/Ti_3C_2 after 1000 cyles; electrochemical impedance spectra with the fitting: (c) CoO/Ti_3C_2, CoO/rGO and CoO (d); (e) XRD of CoO/Ti_3C_2 after cycles.

stem from the incorporation of CoO nanoparticles into few-layer Ti_3C_2, consequently shortening the lithium transfer paths and improving the rate capability and cycling performance [44–46].

4. Conclusion

The cabbage-like CoO/Ti_3C_2 electrode is synthesized by a hydrothermal method and annealing process. The CoO/Ti_3C_2 as an anode has a higher specific capacity of 840.1 $mAhg^{-1}$ at 0.5 C than that of CoO/rGO (798.3 mAh g^{-1} at 0.5C) and CoO (802.4 mAh g^{-1} at 0.5 C) in LIBs. Moreover, the reversible capacity of CoO/Ti_3C_2 is still 598.1 $mAhg^{-1}$ after 1000 cycles, whereas the specific capacity of CoO/rGO (CoO) is lower at 140.1 $mAhg^{-1}$ (260.2 $mAhg^{-1}$) after 600 cycles. The excellent electrochemical characteristics arise from the larger surface area and shorter ion/electron transfer paths. The results indicate the large potential of CoO/Ti_3C_2 as anodes in next-generation LIBs.

CRediT authorship contribution statement

Dajun Wu: Writing – review & editing, Supervision, Resources, Project administration. **Xinyue Zhang:** Writing – original draft, Investigation, Data curation. **Xuan Wan:** Investigation, Formal analysis. **Heng Zhang:** Methodology. **Zhicheng Wang:** Software. **Shi Tao:** Visualization, Software. **Bin Qian:** Validation, Data curation. **Shaohui Xu:** Methodology, Investigation, Data curation. **Paul K. Chu:** Writing – review & editing, Visualization, Funding acquisition.

Declaration of competing interest

The authors declare that they have no known competing financial interests or personal relationships that could have appeared to influence the work reported in this paper.

Acknowledgments

This work was jointly supported by the National Natural Science Foundation of China (Grant No. 11705015, No.62274017), National Science Foundation of Jiangsu Educational Department (Grant No. 15KJA430001), and City University of Hong Kong Donation Research Grants (Grant Nos. 9220061 and DON-RMG 9229021).

References

[1] X. Wang, R. Wang, Q. Kang, L. Yan, T. Ma, D. Li, Y. Xu, H. Ge, Construction of Cu-doped Co_3O_4/rGO composites with a typical buffer structure for high-performance lithium storage, Colloid Surf. A 656 (2023) 130325.
[2] X. Yuan, Z. Ma, S. Jian, H. Ma, Y. Lai, S. Deng, X. Tian, C. Wong, F. Xia, Y. Dong, Mesoporous nitrogen-doped carbon MnO_2 multichannel nanotubes with high performance for Li-ion batteries, Nano Energy 97 (2022) 107235.
[3] X. Du, Y. Ma, W. Zhang, M. Zhang, K. Su, Z. Li, The collaborative effect of Ni_3S_2-NiO heterojunction and porous carbon network modified lithium-sulfur battery separator for effectively inhibiting polysulfides shuttle, J. Power Sources 623 (2024) 235414.
[4] R. Li, A.R. Kamali, Clean preparation of Fe_2SiO_4 coated Fe_2O_3 integrated with graphene for Li-ion storage application, Colloid Surf. A 656 (2023) 130275.
[5] Z. Yan, Z. Sun, K. Yue, A. Li, L. Qian, CoO/ZnO nanoclusters immobilized on N-doped 3 D reduced graphene oxide for enhancing lithium storage capacity, J. Alloys Compd. 836 (2020) 155443.
[6] Y. Li, X. Xiao, L. Zhang, B. Yan, H. Tao, X. Yang, Co@CoO core-shell cross-linked framework modified 3D Cu for dendrite-free lithium anode, Chem. Eng. J. 491 (2024) 151922.
[7] Y. Jiang, M. Du, P. Geng, B. Sun, R. Zhu, H. Pang, CoO/MoO_3 @nitrogen-doped carbon hollow heterostructures for efficient polysulfide immobilization and enhanced ion transport in Lithium-Sulfur batteries, J. Colloid Interface Sci. 664 (2024) 617–625.
[8] X. Li, Q. Chu, M. Song, C. Chen, Y. Li, X. Tian, Y. Cui, D. Zhao, Porous CoO/Co_3O_4 nanoribbons as a superior performance anode material for lithium-ion batteries, Appl. Surf. Sci. 618 (2023) 156658.
[9] W. Kim, D. Shin, B. Seo, S. Chae, H. Cho, E. Jo, W. Choi, Precisely tunable synthesis of binder-free cobalt oxide-based Li-ion battery anode using scalable electrothermal waves, ACS Nano 16 (2022) 17313–17325.
[10] H. Chen, S. Zhang, S. Wu, K. Wang, C. Chen, Y. Chen, W. Chu, Z. Chen, H. Li, H. Liu, Design and synthesis of cellulose nanofiber-derived CoO/Co/C two-dimensional nanosheet toward enhanced and stable lithium storage, J. Colloids Interfaces Sci. 625 (2022) 915–924.
[11] L. Chen, G. Chen, W. Tang, H. Wang, F. Chen, X. Liu, R. Ma, A robust and lithiophilic three-dimension framework of CoO nanorod arrays on carbon cloth for cycling-stable lithium metal anodes, Mater. Today Energy 18 (2020) 100520.
[12] W. Wang, H. Wan, W. Cai, Y. Fang, Z. Fan, Y. Zhu, Y. Qian, The free-standing N-CoO matrix towards optimizing dual-electrodes for high-performance Li-O_2 batteries, Chem. Eng. J. 461 (2023) 142004.
[13] Y. Kim, C. Kim, S. Kim, Y. Kang, D. Lee, G. Park, Fabrication of heteroatom-doped cobalt oxide yolk-shell microsphere using recycled solution from waste materials and their excellent electrochemical properties as an anode material for lithium-ion batteries, Rare Met. 43 (2024) 4934–4947.
[14] B. Wan, J. Guo, W.H. Lai, Y.X. Wang, M. Liu, H.K. Liu, J.Z. Wang, S.L. Chou, S. X. Dou, Layered mesoporous CoO/reduced graphene oxide with strong interfacial coupling as a high-performance anode for lithium-ion batteries, J. Alloys Compd. 843 (2020) 156050.
[15] X. Xiao, H. Chen, J. Tang, L. Wang, CoO@PAN core-sell structure composite as protective layer for stabilizing lithium metal batteries, J. Mater. Sci. Mater. Electron. 34 (2023) 1–13.
[16] Y.F. Yuan, W.C. Zhao, L. Chen, G.S. Cai, S.Y. Guo, CoO hierarchical mesoporous nanospheres@TiO_2@C for high-performance lithium-ion storage, Appl. Surf. Sci. 556 (2021) 149810.
[17] S. Hou, M.N. Liao, Y.Y. Guo, T.Z. Liu, L.K. Wang, J. Li, C. Mei, W.P. Fu, L.Z. Zhao, SiO_2 nanoparticles modulating the “flos albiziae” like CoO by the synergistic effect with enhanced lithium storage, Appl. Surf. Sci. 530 (2020) 147223.
[18] E. Gibertini, F. Lissandrello, L. Bertoli, P. Viviani, L. Magagnin, All-inkjet-printed Ti_3C_2 MXene capacitor for textile energy storage, Coatings 13 (2023) 230.
[19] D. Seo, M.R. Kim, J.K. Song, E. Kim, J. Koo, K.C. Kim, H. Han, Y. Lee, C.W. Ahn, Hollow Ti_3C_2 MXene/carbon nanofibers as an advanced anode material for lithium-ion batteries, ChemElectroChem 9 (2022) 8.
[20] W.Y. Zhang, H.F. Shi, D.H. Wang, J.S. Wang, Z.H. Xiong, C.D. Wang, Y.S. Gu, Z. M. Bai, Q.J. Liang, X.Q. Yan, Three-dimensional Ti_3C_2 MXene@silicon@nitrogen-doped carbon foam for high performance self-standing lithium-ion battery anodes, J. Electroanal. Chem. 921 (2022) 116664.
[21] H. Liu, X. Zhang, Y. Zhu, B. Cao, Q. Zhu, P. Zhang, B. Xu, F. Wu, R. Chen, Electrostatic self-assembly of 0D-2D SnO_2 quantum dots/$Ti_3C_2T_x$ MXene hybrids as anode for lithium-ion batteries, Nano-Micro Lett. 11 (2019) 65.
[22] Y. Jia, J. Liu, L. Shang, Layered structure 2D MXene/TiO_2 composites as high-performance anodes for lithium-ion batteries, Ionics 29 (2023) 531–537.
[23] G.P. Nunna, R. Pitcheri, B.A. Al-Asbah, S. Sangaraju, B. Khan, K.T. Jo, Ti_3C_2 MXene nanosheets/vanadium nitride@carbon composite electrodes for high-performance lithium-ion batteries, Int. J. Energy Res. 2023 (2023) 8091900.
[24] C.Y. Li, D.D. Zhang, J. Cao, P.F. Yu, M. Okhawilai, J. Yi, J.Q. Qin, X.Y. Zhang, Ti_3C_2 MXene-encapsulated NiFe-LDH hybrid anode for high-performance lithium-ion batteries and capacitors, ACS Appl. Energy Mater. 4 (2021) 7821–7828.
[25] J.Q. Liu, S.C. Song, D.C. Zuo, C. Yan, Z.J. He, Y.J. Li, J.C. Zheng, Synthesis and characterization of SiO_2/Ti_3C_2 anode materials for lithium-ion batteries via different methods, Ionics 26 (2020) 5325–5331.
[26] R.C. Wang, Q.L. Pan, Y.H. Luo, C. Yan, Z.J. He, J. Mao, K.H. Dai, X.W. Wu, J. C. Zheng, SnS particles anchored on Ti_3C_2 nanosheets as high-performance anodes for lithium-ion batteries, J. Alloys Compd. 893 (2022) 162089.
[27] S. Zheng, H. Zhou, H. Xue, P. Braunstein, H. Pang, Pillared-layer Ni-MOF nanosheets anchored on Ti_3C_2 MXene for enhanced electrochemical energy storage, J. Colloid Interface Sci. 614 (2022) 130–137.
[28] X. Li, J. Zhu, Y. Fang, W. Lv, F. Wang, Y. Liu, H. Liu, Hydrothermal preparation of CoO/Ti_3C_2 composite material for lithium-ion batteries with enhanced electrochemical performance, J. Electroanal. Chem. 817 (2018) 1–8.
[29] H. Tang, M. Jiang, E. Ren, Y. Zhang, X. Lai, C. Cui, S. Jiang, M. Zhou, Q. Qin, R. Guo, Integrate electrical conductivity and Li^+ ion mobility into hierarchical heterostructure Ti_3C_2@CoO/ZnO composites toward high-performance lithium ion storage, Energy 212 (2020) 118696.
[30] Y. Ren, Q. Zhai, B. Wang, L. Hu, Y. Ma, Y. Dai, S. Tang, X. Meng, Synergistic adsorption-electrocatalysis of 2D/2D heterostructure toward high performance Li-S batteries, Chem. Eng. J. 439 (2022) 135535.
[31] X. Bu, F. Ma, Q. Wu, H. Wu, Y. Yuan, L. Hu, C. Han, X. Wang, W. Liu, X. Li, Metal-organic frameworks-derived Co_3O_4/ $Ti_3C_2T_x$ Mxene nanocomposites for high performance ethanol sensing, Sens. Actuat. B-Chem. 369 (2022) 132232.
[32] C.F. Du, Q. Song, Q. Liang, X. Zhao, J. Wang, R. Zhi, Y. Wang, H. Yu, The passive effect of MXene on electrocatalysis: a Case of $Ti_3C_2T_x$/CoNi-MOF nanosheets for oxygen evolution reaction, ChemNanoMat 7 (2021) 539–544.
[33] N. Kitchamsetti, J.S. Cho, A roadmap of recent advances in MXene@MOF hybrids, its derived composites: synthesis, properties, and their utilization as an electrode for supercapacitors, rechargeable batteries and electrocatalysis, J Energy Storge 80 (2024) 110293.
[34] M. Cui, X. Chen, Z. Wang, S. Tao, D. Wu, B. Qian, L. Wang, P.K. Chu, Fan-shape Mn-doped CoO/C microspheres for high lithium-ion storage capacity, J. Alloy. Compd. 903 (2022) 163980.
[35] P.F. Yan, L. Ji, X.P. Liu, Q.H. Guan, J.L. Guo, Y.L. Shen, H.J. Zhang, W.F. Wei, X. W. Cui, Q. Xu, 2D amorphous-MoO_{3-x}@ Ti_3C_2 -MXene non-van der Waals heterostructures as anode materials for lithium-ion batteries, Nano Energy 86 (2021) 106139.
[36] L. Li, G.X. Jiang, C.H. An, Z.J. Xie, Y.J. Wang, L.F. Jiao, H.T. Yuan, Hierarchical Ti_3C_2 @TiO_2 MXene hybrids with tunable interlayer distance for highly durable lithium-ion batteries, Nanoscale 12 (2020) 10369–10379.
[37] X. Li, C. Wen, H. Li, G. Sun, In situ decoration of nanosized metal oxide on highly conductive MXene nanosheets as efficient catalyst for Li-O_2 battery, J. Energy Chem. 47 (2020) 272–280.
[38] J. Liu, J. Wu, C. Zhou, P. Zhang, G. Shouzhi, S. Li, Y. Yang, K. Li, L. Chen, M. Wang, Single-phase $ZnCo_2O_4$ derived ZnO-CoO mesoporous microspheres encapsulated by nitrogen-doped carbon shell as anode for high-performance lithium-ion batteries, J. Alloy. Compd. 825 (2020) 153951.
[39] Y. Chen, J. Cheng, A. Wang, C. Liu, H. Yan, Y. Qiu, Z. Wang, P.K. Chu, Y. Luo, The enhanced performance of Li-ion batteries based on Co-MOF/MXene composites, Inorg. Chem. Commun. 159 (2024) 111793.
[40] C. Ma, J. Dong, Y. Zhao, J. Li, H. Chen, Dual-template synthesis of novel pomegranate-like hollow carbon nanoparticles with improved electrochemical performance for Li-ion batteries, Carbon 110 (2016) 180–188.
[41] Z.Y. Huang, Y.F. Yuan, Z.C. Lin, J.J. Lin, S.B. Li, S.Y. Guo, Y.Z. Huang, W.W. Yan, Fluffy ultrathin WO_3 nanoneedle clusters in-situ grown in mesoporous hollow carbon nanospheres as advanced anode for lithium-ion batteries, J. Alloy. Compd. 969 (2023) 172458.
[42] J.F. Wang, Y.F. Yuan, Z.C. Lin, J.J. Lin, S.B. Li, Y.Z. Huang, S.Y. Guo, W.W. Yan, Boosting lithium storage performance of Co-Sn double hydroxide nanocubes in-situ grown in mesoporous hollow carbon nanospheres, Electrochim. Acta 465 (2023) 142971.
[43] J.H. Li, Z.S. Xiong, Y.J. Wu, H. Li, X.Y. Liu, H.J. Peng, Y.Y. Zheng, Q. Zhang, Q. B. Liu, Iron (Fe, Ni, Co)-based transition metal compounds for lithium-sulfur batteries: mechanism, progress and prospects, J. Energy Chem. 73 (2022) 513–532.
[44] J.H. Li, Z.Y. Wang, K.X. Shi, Y.J. Wu, W.Z. Huang, Y.G. Min, Q.B. Liu, Z.X. Liang, Nanoreactors encapsulating built-in electric field as a “bridge” for Li–S batteries: directional migration and rapid conversion of polysulfides, Adv. Energy Mater. 14 (2024) 2303546.
[45] J.H. Li, F.Y. Li, J.J. Pan, J.D. Pan, J.Y. Liao, H. Li, H.F. Dong, K.X. Shi, Q.B. Liu, Hollow Co3S4 nanocubes interconnected with carbon nanotubes as nanoreactors to accelerate polysulfide conversion for high-performance lithium–sulfur batteries, Ind. Eng. Chem. Res. 62 (2023) 4364–4372.
[46] Q.B. Liu, Y.J. Wu, D. Li, Y.Q. Peng, X.Y. Liu, B.Q. Li, J.Q. Huang, H.J. Peng, Dilute alloying to implant activation centers in nitride electrocatalysts for lithium–sulfur batteries, Adv. Mater. 35 (2023) 2209233.